Volume 9 | Number 18 | 21 September 2025

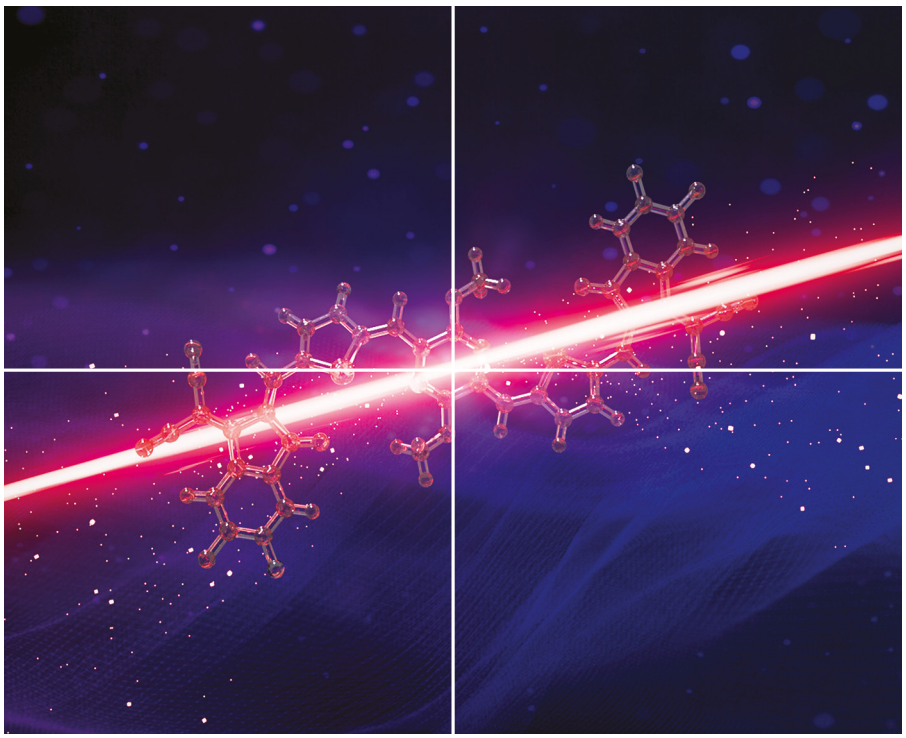

# MATERIALS CHEMISTRY

## FRONTIERS

CCS 中国化学会 CHINESE CHEMICAL SOCIETY

ICCAS 1956

ROYAL SOCIETY OF CHEMISTRY

rsc.li/frontiers-materials

MATERIALS CHEMISTRY FRONTIERS

CHINESE CHEMICAL SOCIETY

ROYAL SOCIETY OF CHEMISTRY

RESEARCH ARTICLE

View Article Online
View Journal | View Issue



Cite this: *Mater. Chem. Front.*, 2025, **9**, 2722

# New *p*-azaquinodimethane core based narrow-gap non-ring fused organic acceptor†

Irene E. Park,[a] Souk Y. Kim,[b] Laura E. Dickson,[c] Pui Mei Helen Tse,[a] Viki Kumar Prasad,[a] Bruno Schmaltz,[d] Benoît H. Lessard,[ce] Nutifafa Y. Doumon[bf] and Gregory C. Welch*[a]

Received 10th May 2025,
Accepted 25th June 2025

DOI: 10.1039/d5qm00355e

rsc.li/frontiers-materials

The design and synthesis of **sAQM-1**, a *para*-azaquinodimethane-based non-ring fused organic π-conjugated molecule with an undemanding, metal-free synthetic route, is reported. **sAQM-1** exhibits a narrow optical gap, stabilized frontier molecular orbitals, strong intramolecular charge transfer, and tunable self-assembly properties. Compared to the ring-fused **Y6** acceptor, electronic energy levels are stabilized, and optical absorption red-shifted, demonstrating the potential of quinoidal scaffolds delivering atom economy and leading to narrow-gap organic electronic materials.



The rapid advancement in organic electronics has been fueled by solution processable π-conjugated organic molecules with highly tunable optoelectronic and structural features.[1] These materials have found broad applications in electronics and photonics.[2] Among these, narrow-gap (<1.6 eV) organic semiconductors are of interest for organic photovoltaics (OPVs),[3] photodetectors (OPDs),[4] and field-effect transistors (OFETs),[5] as they exhibit extended light absorption into the near-infrared (NIR) region in which the NIR photons can be harvested or detected.[3,6]

A common design strategy for narrow-gap materials employs a donor–acceptor (D–A) approach. In this method, donor and acceptor moieties alternate within a π-conjugated backbone, inducing intramolecular charge transfer (ICT), contributing to a quinoidal character and formation of newly hybridized frontier molecular orbitals (Fig. 1(a)).[5] This strategy is further enhanced by increasing molecular coplanarity through ring fusion and non-covalent interactions, improving molar absorptivity and charge-carrier mobility.[6–8]

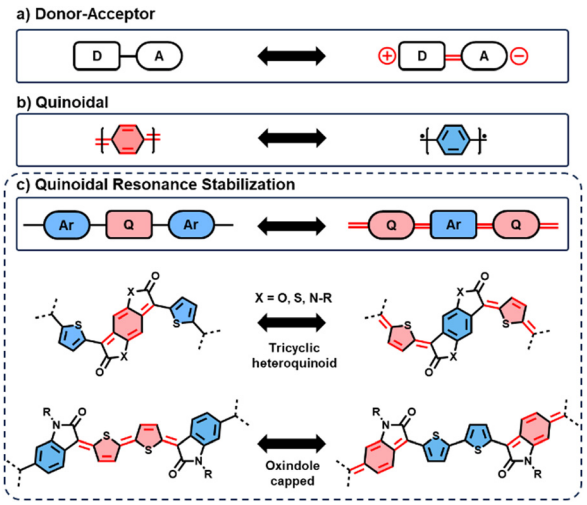


Fig. 1 (a) Donor–acceptor system demonstrating intramolecular charge transfer (ICT). (b) Quinoid (left) and benzenoid (right) resonance forms of *para*-quinodimethane (*p*-QM). (c) Resonance configuration of mixed aromatic/quinoid structures, where Q and Ar indicates quinoidal and aromatic moieties, respectively, and examples structures.

Another alternative strategy is to utilize quinoid molecules, which feature double bonds between the two adjacent molecules, forcing coplanarity within the molecular backbone.[9,10] However, classical quinoidal units such as *para*-quinodimethane (*p*-QM, Fig. 1(b)) suffer from poor ambient stability due to a tendency to adopt reactive open-shell aromatic diradical (benzenoid) forms, which are more energetically favorable than the quinoidal form.[11] This challenge of reactivity can be overcome by stabilizing the quinoidal form by incorporating electron-withdrawing groups or embedding the quinoidal moiety within the π-conjugated backbone.[12] For the latter, there

[a] *Department of Chemistry, University of Calgary, 2500 University Drive N.W., Calgary, Alberta, T2N 1N4, Canada. E-mail: gregory.welch@ucalgary.ca*
[b] *Department of Materials Science and Engineering, The Pennsylvania State University, University Park, PA, 16802, USA*
[c] *Department of Chemical and Biological Engineering, University of Ottawa, 161 Louis Pasteur, Ottawa, Ontario K1N 6N5, Canada*
[d] *Laboratoire de Physico-Chimie des Matériaux et des Electrolytes Pour l'Energie (PCM2E) EA6299, Université de Tours, 37200 Tours, France*
[e] *School of Electrical Engineering and Computer Science, University of Ottawa, 800 King Edward Ave., Ottawa, Ontario K1N 6N5, Canada*
[f] *Department of Engineering Science and Mechanics, The Pennsylvania State University, University Park, PA, 16802, USA*

† Electronic supplementary information (ESI) available. See DOI: https://doi.org/10.1039/d5qm00355e

 

is a balance between the quinoidal and aromatic forms within the conjugated structure (Fig. 1(c)).[13–15] Quinoidal molecules and polymers based on this strategy have been reported and demonstrated exceptional NIR absorption and structural stability. Examples include polycyclic heteroquinoid groups such as benzodifurandione (O),[16–18] benzodipyrrolidone (N-R),[19–22] benzodithiophenedione (S),[23–25] or oxindole-capping,[26–28] and others (Fig. 1(c)).[15,29]

In 2017, Liu *et al.* introduced *p*-azaquinodimethane (*p*-AQM), an ambient-stable quinoidal unit.[30] The stability was established by incorporating heteroatom (nitrogen) and alkoxy group into a *p*-QM scaffold, along with flanking aromatic units (Fig. 2(a)). Additionally, *p*-AQM offers a simple and scalable synthetic route *via* Knoevenagel condensation, avoiding a metal-catalyzed cross-coupling reaction.[31,32] While *p*-AQM has shown promise in creating narrow-gap polymers for applications such as OFETs,[30,33–36] and photothermoelectric devices,[32,37] its potential to afford narrow-gap molecules remains largely unexplored. The broader chemistry of *p*-AQM and its versatility in tuning electronic properties has recently been comprehensively reviewed, further providing its relevance in organic electronics.[38]

One of the state-of-the-art narrow-gap molecules is **Y6** (Fig. 2(b)). This A–D–A′–D–A type fused-ring acceptor has demonstrated exceptional performance in OPVs and OPDs.[39,40] However, synthetic complexity has become a significant hindrance. Multiple organometallic coupling reactions and demanding ring-fusing steps increase production costs and limit scalability.[41] Therefore, the development of non-ring fused molecular acceptors has emerged as an important strategy.[42–47]

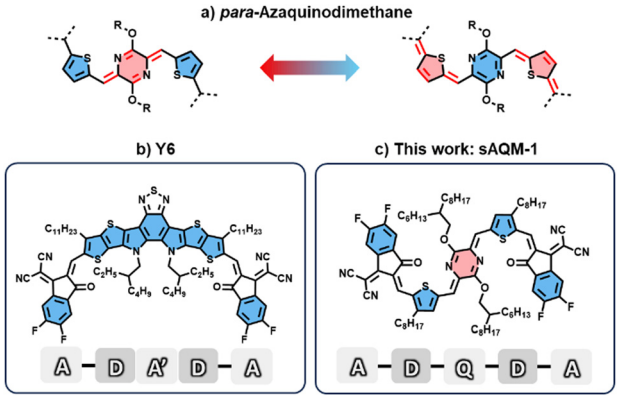


Fig. 2 (a) Quinoid-aromatic resonance forms of *para*-azaquinodimethane (*p*-AQM), chemical structures of (b) **Y6** and (c) this work: **sAQM-1**.

This work presents a non-ring fused *p*-AQM-based acceptor, **sAQM-1**, with an A–D–Q–D–A type structure (Fig. 2(c)). The stabilized quinoidal resonance form of *p*-AQM enables ambient stability, endowing a narrow optical and electrochemical gap while affording a simple atom-economical synthesis.

**sAQM-1** was obtained in a metal-free, four-step synthetic route, as shown in Scheme 1. Commercially available 1,4-diacetylpiperazine-2,5-dione was subjected to Knoevenagel condensation reaction with 4-octylthiophene-2-carboxaldehyde, yielding compound (**1**) with a 39% yield. The low yield is attributed to the impure starting material containing 10% isomer (3-octylthiophene-2-carboxaldehyde). Compound (**1**) was then subjected to an *O*-alkylation reaction using 2-hexadecyl bromide under mild basic conditions, affording compound (**2**) with an 84% yield. This was followed by a Vilsmeier–Haack formylation reaction to obtain compound (**3**) with a 75% yield. It should be noted that without the side chain on the thiophene moiety, the *O*-alkylated product exhibits topochemical activity, undergoing heat- or light-induced solid-state polymerization. This behavior aligns with reports of *p*-AQM molecules that undergo topochemical polymerization depending on the extent of end-group aromaticity,[48] end-group substituents,[49] and the proximity of reactive methylene groups.[50] In this case, installing a side chain on the thiophene suppresses such reactivity. Finally, **sAQM-1** was obtained through a Knoevenagel condensation reaction between compound (**3**) and the endcap, 2-(5,6-difluoro-3-oxo-2,3-dihydro-1*H*-inden-1-ylidene) malononitrile, yielding the final product with a 93% yield. The chemical structure of **sAQM-1** was fully characterized using $^{1}$H and $^{13}$C NMR spectroscopy, high-resolution mass spectrometry, and CHN elemental analysis (Fig. S7, S8, S12 and S13, ESI†). Details about the synthesis and characterizations for each compound are available in ESI.†

Thiophene-flanked *p*-AQM has been reported to favor intramolecular S···N interactions, enhancing coplanarity by reducing rotational freedom.[30] Additionally, the introduction of additional vinylic bridges, such as those from the endcap, can further enhance backbone planarity.[33] To probe the molecular conformation of **sAQM-1**, a variable-temperature (VT) $^{1}$H-NMR spectroscopic experiment was performed in 1,1,2,2-tetrachloroethane-$d_2$ (Fig. S14 and S15, ESI†). As the temperature increased from 21 °C to 120 °C, all resonances shifted upfield. Additionally, no broadening or coalescence was observed. The observed upfield shift is attributed to the disruption of intermolecular interactions rather than intramolecular rotation. Although the VT-$^{1}$H NMR spectroscopic experiment does not provide direct insight into the molecular

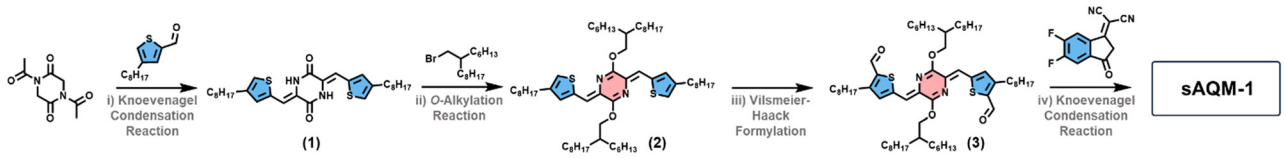


Scheme 1 Synthesis schematics for **sAQM-1**. (i) $NEt_3$, DMF, 120 °C, overnight (39%), (ii) $K_2CO_3$, DMF, 120 °C, 2.5 hours (84%), (iii) $POCl_3$, DMF, $CH_2Cl_2$, 65 °C, 16 hours (75%), (iv) pyridine, $CHCl_3$, 65 °C, overnight (93%).

conformation of **sAQM-1**, the absence of spectral changes suggests that it adopts a fixed and rigid conformation across all temperatures, unlike non-ring fused molecules with rotatable single C–C bonds.[43,51] The density functional theory (DFT) calculations also show that the S···N non-covalent interaction in the *Z*,*Z* isomer leads to a more favorable conformation, which is more stable than the *E*,*E* isomer, in line with the literature (Fig. S16, ESI†).[30,31]

Owing to the structural rigidity, **sAQM-1** has lower solubility than expected. Nevertheless, it can be solubilized in solvents such as chlorobenzene, chloroform, *o*-dichlorobenzene, and *o*-xylene upon heating at 65 °C at 5 mg $mL^{-1}$. However, the compound forms needle-like crystallites over time when returned to room temperature, demonstrating a tendency to aggregate (Fig. S17, ESI†). To further study intermolecular interactions of **sAQM-1**, concentration-dependent $^1$H-NMR was performed in $CDCl_3$ (Fig. S18 and S19, ESI†). As the concentration increases from 0.5 to 5 mg $mL^{-1}$, the aromatic protons are shifted downfield, while aliphatic protons show no obvious change. The downfield shift of aromatic protons is attributed to the ring current effects resulting from the increased π–π stacking interactions,[52] with methylene proton adjacent to the *p*-AQM core showing the most prominent shift at about 0.07 ppm, indicating extensive intermolecular interactions (Fig. S18, ESI†).

The thermal behavior of **sAQM-1** was determined using differential scanning calorimetry (DSC, Fig. S20 and S21, ESI†) and compared to **Y6**. The first heating of **Y6** exhibits a sharp endothermic melting point ($T_m$) at 294.5 °C, consistent with previous reports (Fig. S20a, ESI†).[53,54] In contrast, the cooling scan of **Y6** shows no distinct exothermic crystallization peak ($T_c$), likely due to its slow crystallization kinetics arising from the large fused backbone and complex molecular structure.[55,56] As a result, the second DSC cycle of **Y6** shows no thermal transition (Fig. S21a, ESI†). For **sAQM-1**, the second DSC cycle displays sharp endothermic and exothermic transitions at 222.6 °C and 205.0 °C, respectively (Fig. S21b, ESI†). These distinct transitions indicate that **sAQM-1** possesses high structural rigidity. Such behavior is similar to related molecules with D–A structures incorporating conformational locks.[57–59]

The electronic properties of **sAQM-1** were examined using solution cyclic voltammetry (CV) in $CH_2Cl_2$ and compared to **Y6** (Fig. 3(a), Fig. S22 and Table S1, ESI†). Note that solution CV has resulted in discrepancies with **Y6** energy levels from the literature, as they are reported using CV in film.[39] **Y6** exhibits an irreversible first reduction process, whereas **sAQM-1** shows reversible reduction. Conversely, the first oxidation process is reversible for **Y6** and quasi-reversible for **sAQM-1**. The first reduction occurs at −0.93 V ($E^{red}_{onset}$) for **Y6** and −0.77 V ($E^{red}_{1/2}$) for **sAQM-1** (*vs.* $Fc/Fc^+$), while the oxidation occurs at 0.61 V ($E^{ox}_{1/2}$) for **Y6** and 0.59 V ($E^{ox}_{onset}$) for **sAQM-1** (*vs.* $Fc/Fc^+$).

The optical properties of **sAQM-1** were studied by optical absorption spectroscopy and directly compared with **Y6** (Fig. 3(b)). In $CHCl_3$ solution, both **Y6** and **sAQM-1** exhibit sharp vibronic peaks (0-0 and 0-1) in the low-energy absorption band.[60] The absorption peaks for **Y6** are located at 734 and 672 nm, respectively, with a molar extinction coefficient ($\varepsilon^{sol}_{abs}$) of $1.7 \times 10^5$ $M^{-1}$ $cm^{-1}$, while **sAQM-1** exhibits peaks at 782 and 714 nm, respectively, with $\varepsilon^{sol}_{abs}$ of $1.3 \times 105$ $M^{-1}$ $cm^{-1}$ (Fig. S23 and S24, ESI†). The presence of sharp vibronic peaks and relatively high $\varepsilon^{sol}_{abs}$ suggest that both molecules maintain a rigid and planar conformation in solution, resulting in enhanced intermolecular interactions and ICT effect.[61] **sAQM-1** has a narrower optical gap ($E^{opt}_g$) than **Y6**, with the 0-0 peak and absorption onset red-shifted relative to **Y6** by 51 nm and 48 nm, respectively.

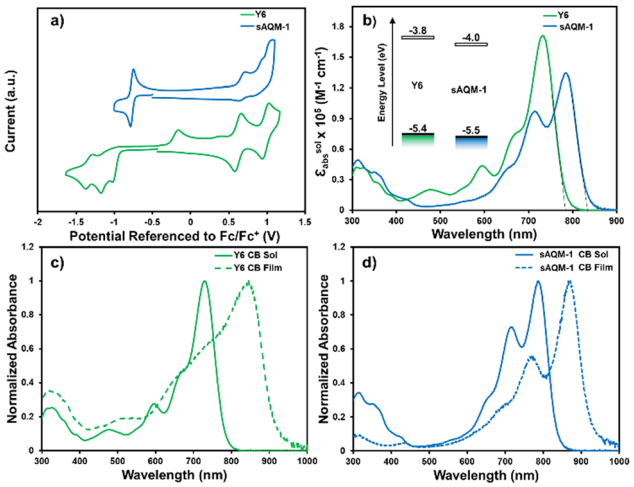


Fig. 3 (a) Cyclic voltammogram of **Y6** (green) and **sAQM-1** (blue). CVs were measured in $CH_2Cl_2$ solution under $N_2$ referenced to the $Fc/Fc^+$ couple (Fc: ferrocene), recorded at 100 mV $s^{-1}$. (b) Absorption spectra of **Y6** and **sAQM-1** solution in $CHCl_3$ (CF). (Inset) Energy level diagram of **Y6** and **sAQM-1**. Normalized optical absorption spectrum of (c) **Y6** and (d) **sAQM-1** chlorobenzene (CB) solution (solid line) and annealed chlorobenzene (CB) spin-cast film at 150 °C for 10 minutes (dotted line).

The calculated energy gap ($E^{CV}_g$) follows the same trend as $E^{opt}_g$, supporting that **sAQM-1** has a narrower gap than **Y6.** Using $E^{ox}_{1/2}$ value (or $E_{LUMO} - E^{opt}_g$, if oxidation is not reversible), the highest occupied molecular orbital energy level ($E_{HOMO}$) was estimated to be −5.4 eV for **Y6** and −5.5 eV for **sAQM-1** (Fig. 3(b)). The lowest unoccupied molecular orbital energy level ($E_{LUMO}$) was estimated using $E^{red}_{1/2}$ value (or $E_{HOMO} + E^{opt}_g$, if reduction is not reversible), yielding −3.8 eV for **Y6** and −4.0 eV for **sAQM-1** (Fig. 3(b)). Overall, **sAQM-1** exhibits more stabilized frontier molecular orbital energy levels and a smaller energy gap than **Y6**, thus indicating that the quinoidal conjugation strategy is effective at mimicking the properties of ring-fused systems. The optoelectronic data are summarized in Table 1.

The photoluminescence (PL) spectra of **Y6** and **sAQM-1** were measured in chlorobenzene (CB), chloroform (CF), dichlorobenzene (*o*-DCB), and *o*-xylene (Fig. S25, ESI†). Both molecules exhibit polarity-dependent absorption and emission, indicative of a strong ICT effect.[62] The Stokes shift, which represents the energy loss during the transition between the ground and excited states, was calculated from the difference between maximum absorption ($\lambda^{sol}_{max}$) and emission energies (Table S2, ESI†).

 

Table 1 Experimental optoelectronic properties of **Y6** and **sAQM-1**

| Compound | Absorption spectra | | | Cyclic voltammetry | | | Energy level | |
|---|---|---|---|---|---|---|---|---|
| | $\lambda_{max}^{sol}$ [a] [nm] | $\lambda_{onset}^{sol}$ [b] [nm] | $E_g^{opt}$ [c] [eV] | $E_{1/2}^{red}$ [V] | $E_{1/2}^{ox}$ [V] | $E_g^{CV}$ [d] [eV] | $E_{LUMO}$ [e] [eV] | $E_{HOMO}$ [f] [eV] |
| **Y6** | 734 | 784 | 1.58 | −0.93[g] | 0.61 | 1.54 | −3.83 | −5.41 |
| **sAQM-1** | 782 | 832 | 1.49 | −0.77 | 0.59[g] | 1.36 | −4.03 | −5.52 |

[a] Absorption maximum in chloroform solution ($\sim 10^{-5}$ M). [b] Onset absorption edge of solutions. [c] Optical bandgap calculated from the onset absorption edge of solutions, calculated by $E_g^{opt} = 1240/\lambda_{onset}^{sol}$. [d] Energy bandgap calculated from solution cyclic voltammetry using the first $E_{1/2}$ or $E_{onset}$ values for reduction and oxidation. [e] Calculated by $E_{LUMO} = -4.8$ eV $- E_{1/2}^{red}$, if not reversible, $E_{LUMO} = E_{HOMO} + E_g^{opt}$. [f] Calculated by $E_{HOMO} = -4.8$ eV $- E_{1/2}^{ox}$, if not reversible, $E_{HOMO} = E_{LUMO} - E_g^{opt}$. [g] Indicates for the $E_{onset}$ value for the reduction or oxidation due to their quasi-reversibility or irreversibility.

**sAQM-1** had smaller Stokes shift compared to **Y6** by 0.04, 0.01, 0.06, and 0.04 eV in CB, CF, *o*-DCB, and *o*-xylene, respectively, suggesting a lower energy loss through nonradiative decay, again, likely due to a more rigid molecular conformation. Smaller excited-state relaxation correlates with reduced reorganization energy, which can enhance exciton lifetime and diffusion length.[63]

**Y6** films spin-casted from CB solutions show significantly broadened absorption and a ~100 nm redshift in the 0-0 peak after annealing (Fig. 3(c)). This broadening is attributed to multiple packing modes between the end groups and units.[64] These packing interactions facilitate the formation of a 3D network, resulting in enhanced charge transport in multiple directions.[65,66] In contrast, annealed **sAQM-1** spin-casted films from CB show sharp, red-shifted vibronic peaks at 0-0 and 0-1 by ~83 and 52 nm, respectively, without significant broadening (Fig. 3(d) and Fig. S26, ESI†). The high 0-0/0-1 ratio combined with red-shifted absorption suggests enhanced π–π intermolecular interactions and dominant J-type aggregation in the solid state, while minimal broadening indicates the lack of variation in packing modes.[67]

Notably, **sAQM-1** exhibits drastically different self-assembly behavior when processed from CF. The as-cast film shows a low 0-0/0-1 transition ratio, with the 0-0 and 0-1 peaks at ~857 nm and ~743 nm, respectively. Upon annealing up to 120 °C, the 0-0/0-1 ratio increases (Fig. S27, ESI†). However, at a higher temperature, the 0-0 peak and absorption onset are slightly blue shifted by ~15 nm, and a new peak appears at 630 nm (Fig. S27, ESI†). These observations suggest that **sAQM-1** may adopt an H-aggregated structure. The aggregation type can be tuned using solvent additives during the film forming and annealing process. For example, adding 1% CB or 1-chloronaphthalene (CN) additives in CF solution during film formation promotes J-aggregation, giving a red-shifted optical profile, 1% 1,8-diiodooctane (DIO) and diphenyl ether (DPE) has no noticeable effects (Fig. S28, ESI†). Therefore, this smart solvent addition presents a unique opportunity to control molecular self-assembly.

Synchrotron-based grazing-incidence wide-angle X-ray scattering (GIWAXS) analysis further supports this observation, as

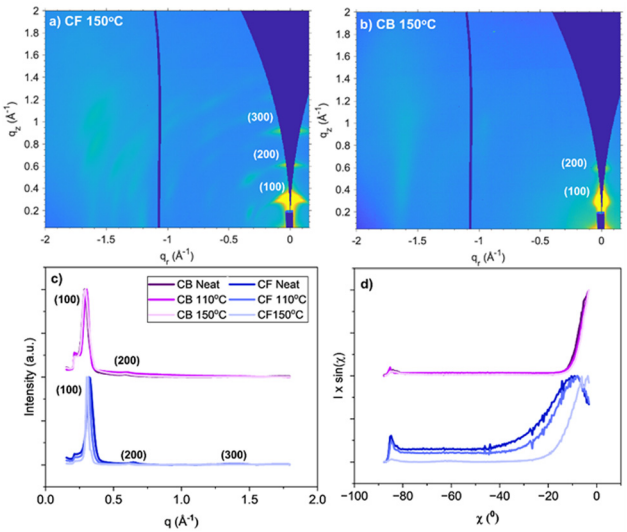


Fig. 4 (a) and (b) 2D GIWAXS patterns ($\theta$ = 0.15°) for **sAQM-1** films cast from (a) CF and (b) CB, after annealing at 150 °C. (c) Corresponding azimuthally integrated diffraction patterns. (d) Azimuthal ($\chi$) linecut profiles for CF- and CB-cast films, integrated over a $q$ range of 0.2–0.4 Å$^{-1}$.

demonstrated by the 2D scattering pattern (Fig. 4(a) and (b)), azimuthally integrated diffraction profiles (Fig. 4(c)), and $\chi$-dependent linecut profiles (Fig. 4(d)). In these experiments, **sAQM-1** was spin-coated onto silicon substrates at 3000 rpm from either CB or CF solutions. The resulting films were analyzed in their as-cast (neat) state or after thermal annealing at 110 °C or 150 °C for 10 minutes.

The scattering spectra reveals that films are moderately semicrystalline, with both exhibiting a dominant, high-intensity (100) reflection at approximately $q$ = 0.2 Å$^{-1}$. Films cast using CB show tendency for increased interplanar spacing ($d_{100} \approx 21.36$ Å) compared to those cast with CF ($d_{100} \approx 20.05$ Å) (Table S3, ESI†). Additionally, CF-cast films exhibit multiple packing modes ($q_{200}$ and $q_{300}$, Fig. 4(a) and (b)) that are more disordered than those observed in CB-cast films. This is better illustrated in Fig. 4(d), where the broadening of the high-intensity peak at $\chi = -8°$ for CF films indicates mixed orientations within the (100) packing structure. Upon annealing, this distribution narrows, suggesting that increased thermal treatment promotes more ordered molecular packing (Fig. S29, ESI†). In contrast, CB-cast films display a narrower distribution consistent with a single preferred orientation, aligning with the absorption spectra that shows minimal variation in the packing modes and orientations of **sAQM-1** when processed with CB.

Electron mobility was measured using electron-only devices to evaluate the electron transport properties of **sAQM-1**. Although **sAQM-1** may indicate superior performance when processed in solvents such as CB and *o*-xylene, CF and CF + 1 vol% CB were selected to ensure consistency in film thickness and compatibility with the processing conditions used for the benchmark material, **Y6**, cast from CF.[39,68] Electron mobility was extracted by analyzing the dark *J*–*V* characteristics using the Murgatroyd relation for the single-carrier space charge

limited current (SCLC) method:

$$J_{SCL} = \frac{9}{8}\varepsilon_r\varepsilon_0\mu\frac{V^2}{L^3}\exp\left(\frac{0.89\beta}{\sqrt{L}}\sqrt{V_{in}}\right)$$

where $J_{SCL}$ is the current density, $\mu$ is the carrier mobility, $\varepsilon_r$ is the relative permittivity, $\varepsilon_0$ is vacuum permittivity, $L$ is the thickness of the device, and $\beta$ is the field activation factor.[69–71] Since film thickness influences mobility, electron-only devices were fabricated using two spin speeds, 1000 rpm (1k) and 2000 rpm (2k), for both **Y6** and **sAQM-1** to enable a consistent comparison. The corresponding film thicknesses for each condition are provided in Table S4 in the ESI.† As shown in Fig. 5(a), the benchmark material **Y6** exhibits an average electron mobility of around $1 \times 10^{-4}$ $cm^2$ $V^{-1}$ $s^{-1}$ to $1 \times 10^{-5}$ $cm^2$ $V^{-1}$ $s^{-1}$, consistent with the values reported in the literature.[39,68] In comparison, **sAQM-1** devices show relatively lower initial electron mobility of around $5 \times 10^{-7}$ $cm^2$ $V^{-1}$ $s^{-1}$ for devices processed in CF and between $10^{-7}$ and $10^{-8}$ $cm^2$ $V^{-1}$ $s^{-1}$ for devices processed in CF + 1 vol% CB. Interestingly, after illumination, the electron mobilities of **sAQM-1** increased significantly to about $2 \times 10^{-5}$ $cm^2$ $V^{-1}$ $s^{-1}$ for devices processed in CF and between $10^{-6}$ and $10^{-7}$ $cm^2$ $V^{-1}$ $s^{-1}$ for devices processed in CF + 1 vol% CB, representing an improvement of about two orders and one order of magnitude, respectively (Fig. 5(b)). In contrast, the increase in mobility for **Y6** was less than one order of magnitude. This is confirmed with at least 5 different devices, as shown in Fig. S30 (ESI†), with the best and average values shown in Table S4 (ESI†). This enhancement in mobility for **sAQM-1** can be attributed to light soaking effect, commonly observed in metal oxides like $SnO_2$,[72,73] and interaction between $SnO_2$ and **sAQM-1** layer, which may be unfavorable in the fresh device state. This pronounced improvement in **sAQM-1** electron mobility suggests that with further optimization in structural modifications, processing, and solid-state properties, this molecular scaffold has the potential to achieve high mobilities comparable to **Y6** in the fresh state. Furthermore, the higher mobility of **sAQM-1** processed in CF suggests the H-aggregated structure, in this case, may lead to better electronic performance.

In conclusion, this work presents the design and synthesis of **sAQM-1**, a quinoidal non-ring fused small-molecule based on *p*-AQM core, using a simple and metal-free four-step synthesis route. **sAQM-1** exhibits optoelectronic properties similar to the state-of-the-art fused-ring acceptor **Y6**, including a narrow optical and electrochemical gap. Structural characterization suggests that **sAQM-1** adopts a rigid and planar conformation with strong intermolecular interactions and structural rigidity, attributed to a stabilized quinoidal resonance form and conformational locks. The aggregation mode can be tunable through a careful selection of solvents and additives. Overall, this study demonstrates the potential of stabilized quinoidal cores like *p*-AQM as versatile scaffolds to create near-IR absorbing molecules. Future work will focus on structural tuning to further modulate energy levels, solubility, and self-assembly properties, with the goal of achieving anisotropic charge transport, like **Y6**, with potential applications in organic photodetectors, photovoltaics, and related optoelectronic devices.

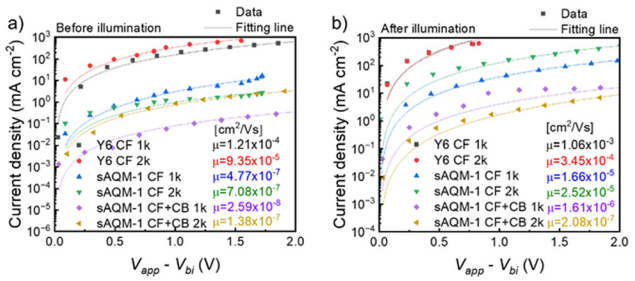


Fig. 5 Dark *J*–*V* characteristics of electron-only devices based on **Y6** and **sAQM-1** for electron mobility extraction using the modified Mott–Gurney law (SCLC method): (a) before and (b) after continuous illumination at 100 mW $cm^{-2}$ for 18 hours in a nitrogen environment. **Y6** and **sAQM-1** layers for devices were processed in CF and CF + 1 vol% CB using two different spin speeds: 1000 rpm (1k) and 2000 rpm (2k).

I. E. P. thanks Alberta Innovates for scholarships. V. K. P. would like to thank Advanced Research Computing at the University of Calgary for providing computational resources. G. C. W. acknowledges funding from the NSERC DG program (2019-04382), the Canada Foundation for Innovation, and the University of Calgary.

## Conflicts of interest

There are no conflicts to declare.

## Data availability

The data supporting this article have been included as part of the ESI.† This data includes NMR spectra, mass spectra, elemental analysis data sheets, DSC plots, and mobility data.

## Notes and references

1 C. Kunkel, J. T. Margraf, K. Chen, H. Oberhofer and K. Reuter, Active discovery of organic semiconductors, *Nat. Commun.*, 2021, 2422.
2 R. Iftikhar, F. Z. Khan and N. Naeem, Recent synthetic strategies of small heterocyclic organic molecules with optoelectronic applications: a review, *Mol. Diversity*, 2024, **28**, 271–307.
3 P. Cheng and Y. Yang, Narrowing the Band Gap: The Key to High-Performance Organic Photovoltaics, *Acc. Chem. Res.*, 2020, **53**, 1218–1228.
4 Q. Li, Y. Guo and Y. Liu, Exploration of Near-Infrared Organic Photodetectors, *Chem. Mater.*, 2019, **31**, 6359–6379.
5 L. Dou, Y. Liu, Z. Hong, G. Li and Y. Yang, Low-Bandgap Near-IR Conjugated Polymers/Molecules for Organic Electronics, *Chem. Rev.*, 2015, **115**, 12633–12665.
6 C. Liu, K. Wang, X. Gong and A. J. Heeger, Low bandgap semiconducting polymers for polymeric photovoltaics, *Chem. Soc. Rev.*, 2016, **45**, 4825–4846.
7 B. Schweda, M. Reinfelds, P. Hofstadler, G. Trimmel and T. Rath, Recent Progress in the Design of Fused-Ring Non-

Fullerene Acceptors—Relations between Molecular Structure and Optical, Electronic, and Photovoltaic Properties, *ACS Appl. Energy Mater.*, 2021, **4**, 11899–11981.

8 Q. Bai, Q. Liang, H. Li, H. Sun, X. Guo and L. Niu, Recent progress in low-cost noncovalently fused-ring electron acceptors for organic solar cells, *Aggregate*, 2022, **3**, e281.

9 J. L. Brédas, Relationship between band gap and bond length alternation in organic conjugated polymers, *J. Chem. Phys.*, 1985, **82**, 3808–3811.

10 J. L. Brédas, Theoretical design of polymeric conductors, *Synth. Met.*, 1987, **17**, 115–121.

11 J. Casado, Para-Quinodimethanes: A Unified Review of the Quinoidal-Versus-Aromatic Competition and its Implications, *Top. Curr. Chem.*, 2017, **375**, 73.

12 Y. Mok, Y. Kim, Y. Moon, J.-J. Park, Y. Choi and D.-Y. Kim, Quinoidal Small Molecule Containing Ring-Extended Termini for Organic Field-Effect Transistors, *ACS Omega*, 2021, **6**, 27305–27314.

13 N. Bérubé, J. Gaudreau and M. Côté, Low Band Gap Polymers Design Approach Based on a Mix of Aromatic and Quinoid Structures, *Macromol.*, 2013, **46**, 6873–6880.

14 Z. X. Chen, Y. Li and F. Huang, Persistent and Stable Organic Radicals: Design, Synthesis, and Applications, *Chem*, 2021, **7**, 288–332.

15 J. Huang and G. Yu, Recent progress in quinoidal semiconducting polymers: structural evolution and insight, *Mater. Chem. Front.*, 2021, **5**, 76–96.

16 T. Lei, J.-H. Dou, X.-Y. Cao, J.-Y. Wang and J. Pei, Electron-Deficient Poly(*p*-phenylene vinylene) Provides Electron Mobility over 1 $cm^2\ V^{-1}\ s^{-1}$ under Ambient Conditions, *J. Am. Chem. Soc.*, 2013, **135**, 12168–12171.

17 Z. Yan, B. Sun and Y. Li, Novel stable (3*E*,7*E*)-3,7-bis(2-oxoindolin-3-ylidene)benzo[1,2-*b*:4,5-*b*′]difuran-2,6(3*H*,7*H*)-dione based donor–acceptor polymer semiconductors for n-type organic thin film transistors, *Chem. Commun.*, 2013, **49**, 3790–3792.

18 D. R. Hinojosa, N. J. Pataki, P. Rossi, A. Erhardt, S. Guchait, F. Pallini, C. McNeill, C. Müller, M. Caironi and M. Sommer, Solubilizing Benzodifuranone-Based Conjugated Copolymers with Single-Oxygen-Containing Branched Side Chains, *ACS Appl. Polym. Mater.*, 2024, **6**, 457–465.

19 W. Cui and F. Wudl, Dithienylbenzodipyrrolidone: New Acceptor for Donor–Acceptor Low Band Gap Polymers, *Macromol.*, 2013, **46**, 7232–7238.

20 K. C. Lee, W.-T. Park, Y.-Y. Noh and C. Yang, Benzodipyrrolidone (BDP)-Based Polymer Semiconductors Containing a Series of Chalcogen Atoms: Comprehensive Investigation of the Effect of Heteroaromatic Blocks on Intrinsic Semiconducting Properties, *ACS Appl. Mater. Interfaces*, 2014, **6**, 4872–4882.

21 H. Zhang, S. Ying, B. Tieke, J. Zhang and W. Yang, 1,6-Naphthodipyrrolidone-based donor–acceptor polymers with low bandgap, *Polymer*, 2015, **60**, 215–220.

22 M. Yang, B. Yin, G. Hu, Y. Cao, S. Lu, Y. Chen, Y. He, X. Yang, B. Huang, J. Li, B. Wu, S. Pang, L. Shen, Y. Liang, H. Wu, L. Lan, G. Yu, F. Huang, Y. Cao and C. Duan, Sensitive short-wavelength infrared photodetection with a quinoidal ultralow band-gap n-type organic semiconductor, *Chem*, 2024, **10**, 1425–1444.

23 K. Kawabata, M. Saito, I. Osaka and K. Takimiya, Very Small Bandgap π-Conjugated Polymers with Extended Thienoquinoids, *J. Am. Chem. Soc.*, 2016, **138**, 7725–7732.

24 K. Kawabata, I. Osaka, M. Sawamoto, J. L. Zafra, P. Mayorga Burrezo, J. Casado and K. Takimiya, Dithienyl Acenedithiophenediones as New π-Extended Quinoidal Cores: Synthesis and Properties, *Chem. – Eur. J.*, 2017, **23**, 4579–4589.

25 K. Kawabata and K. Takimiya, Quinoid-Aromatic Resonance for Very Small Optical Energy Gaps in Small-Molecule Organic Semiconductors: A Naphthodithiophenedione-oligothiophene Triad System, *Chem. – Eur. J.*, 2021, **27**, 15660–15670.

26 H. Hwang, D. Khim, J. Yun, E. Jung, S. Jang, Y. H. Jang, Y. Noh and D. Kim, Quinoidal Molecules as a New Class of Ambipolar Semiconductor Originating from Amphoteric Redox Behavior, *Adv. Funct. Mater.*, 2015, **25**, 1146–1156.

27 H. Hwang, Y. Kim, M. Kang, M.-H. Lee, Y.-J. Heo and D.-Y. Kim, A conjugated polymer with high planarity and extended π-electron delocalization *via* a quinoid structure prepared by short synthetic steps, *Polym. Chem.*, 2017, **8**, 361–365.

28 Y. Kim, Y.-J. Kim, Y.-A. Kim, E. Jung, Y. Mok, K. Kim, H. Hwang, J.-J. Park, M.-G. Kim, S. Mathur and D.-Y. Kim, Open-Shell and Closed-Shell Quinoid–Aromatic Conjugated Polymers: Unusual Spin Magnetic and High Charge Transport Properties, *ACS Appl. Mater. Interfaces*, 2021, **13**, 2887–2898.

29 L. Li, T. Li and Y. Lin, Organic photovoltaic materials with near-infrared II-region response, *Giant*, 2024, **20**, 100334.

30 X. Liu, B. He, C. L. Anderson, J. Kang, T. Chen, J. Chen, S. Feng, L. Zhang, M. A. Kolaczkowski, S. J. Teat, M. A. Brady, C. Zhu, L.-W. Wang, J. Chen and Y. Liu, *para*-Azaquinodimethane: A Compact Quinodimethane Variant as an Ambient Stable Building Block for High-Performance Low Band Gap Polymers, *J. Am. Chem. Soc.*, 2017, **139**, 8355–8363.

31 W. Zwaihed, F. Maurel, M. Kobeissi and B. Schmaltz, New Quinoid Bio-Inspired Materials Using Para-Azaquinodimethane Moiety, *Molecules*, 2023, **29**, 186.

32 M. Li, Y. Xiao, P. Deng and Y. Yu, Near-Infrared Absorbing Para-Azaquinodimethane Conjugated Polymers Synthesized *via* the Transition-Metal-Free Route toward Efficient Photothermal Conversion, *Macromol. Rapid Commun.*, 2024, **45**, 2300648.

33 B. Dyaga, S. Mayarambakam, O. A. Ibraikulov, N. Zimmermann, S. Fall, O. Boyron, T. Heiser, N. Leclerc, N. Berton and B. Schmaltz, *para*-Azaquinodimethane based quinoidal polymers for opto-electronic applications: impact of donor units on the opto-electronic properties, *Mater. Adv.*, 2022, **3**, 6853–6861.

34 Y. Xiao, H. Fu, Z. Li, Y. Zheng, P. Deng, Y. Lei and Y. Yu, 6*H*-[1,2,5]Thiadiazolo[3,4-*e*]thieno[3,2-*b*]indole-flanked *para*-azaquinodimethane based aromatic-quinoidal polymer

semiconductors with high molecular weights synthesized *via* direct arylation polycondensation, *Mater. Adv.*, 2023, **4**, 1927–1934.

35 H. Liang, C. Liu, Z. Zhang, X. Liu, Q. Zhou, G. Zheng, X. Gong, L. Xie, C. Yang, L. Zhang, B. He, J. Chen and Y. Liu, Unravelling the Role of Electron Acceptors for the Universal Enhancement of Charge Transport in Quinoid–Donor–Acceptor Polymers for High-Performance Transistors, *Adv. Funct. Mater.*, 2022, **32**, 2201903.

36 C. Liu, X. Liu, G. Zheng, X. Gong, C. Yang, H. Liu, L. Zhang, C. L. Anderson, B. He, L. Xie, R. Zheng, H. Liang, Q. Zhou, Z. Zhang, J. Chen and Y. Liu, An unprecedented quinoid–donor–acceptor strategy to boost the carrier mobilities of semiconducting polymers for organic field-effect transistors, *J. Mater. Chem. A*, 2021, **9**, 23497–23505.

37 C. L. Anderson, N. Dai, S. J. Teat, B. He, S. Wang and Y. Liu, Electronic Tuning of Mixed Quinoidal-Aromatic Conjugated Polyelectrolytes: Direct Ionic Substitution on Polymer Main-Chains, *Angew. Chem., Int. Ed.*, 2019, **58**, 17978–17985.

38 X. Liu, C. L. Anderson and Y. Liu, *p*-Azaquinodimethane: A Versatile Quinoidal Moiety for Functional Materials Discovery, *Acc. Chem. Res.*, 2023, **56**, 1669–1682.

39 J. Yuan, Y. Zhang, L. Zhou, G. Zhang, H.-L. Yip, T.-K. Lau, X. Lu, C. Zhu, H. Peng, P. A. Johnson, M. Leclerc, Y. Cao, J. Ulanski, Y. Li and Y. Zou, Single-Junction Organic Solar Cell with over 15% Efficiency Using Fused-Ring Acceptor with Electron-Deficient Core, *Joule*, 2019, **3**, 1140–1151.

40 B. Xie, R. Xie, K. Zhang, Q. Yin, Z. Hu, G. Yu, F. Huang and Y. Cao, Self-filtering narrowband high performance organic photodetectors enabled by manipulating localized Frenkel exciton dissociation, *Nat. Commun.*, 2020, **11**, 2871.

41 D. Luo, C. J. Brabec and A. K. K. Kyaw, Non-fused ring electron acceptors for high-performance and low-cost organic solar cells: Structure-function, stability and synthesis complexity analysis, *Nano Energy*, 2023, **114**, 108661.

42 S. Li, L. Zhan, F. Liu, J. Ren, M. Shi, C.-Z. Li, T. P. Russell and H. Chen, An Unfused-Core-Based Nonfullerene Acceptor Enables High-Efficiency Organic Solar Cells with Excellent Morphological Stability at High Temperatures, *Adv. Mater.*, 2018, **30**, 1705208.

43 Z.-P. Yu, Z.-X. Liu, F.-X. Chen, R. Qin, T.-K. Lau, J.-L. Yin, X. Kong, X. Lu, M. Shi, C.-Z. Li and H. Chen, Simple non-fused electron acceptors for efficient and stable organic solar cells, *Nat. Commun.*, 2019, **10**, 2152.

44 J. Wang, C. Wang, Y. Wang, J. Qiao, J. Ren, J. Li, W. Wang, Z. Chen, Y. Yu, X. Hao, S. Zhang and J. Hou, Pyrrole-Based Fully Non-fused Acceptor for Efficient and Stable Organic Solar Cells, *Angew. Chem., Int. Ed.*, 2024, **63**, e202400565.

45 L. Ma, S. Zhang, J. Zhu, J. Wang, J. Ren, J. Zhang and J. Hou, Completely non-fused electron acceptor with 3D-interpenetrated crystalline structure enables efficient and stable organic solar cell, *Nat. Commun.*, 2021, **12**, 5093.

46 N. Yang, Y. Cui, Y. Xiao, Z. Chen, T. Zhang, Y. Yu, J. Ren, W. Wang, L. Ma and J. Hou, Completely Non-Fused Low-Cost Acceptor Enables Organic Photovoltaic Cells with 17% Efficiency, *Angew. Chem., Int. Ed.*, 2024, **63**, e202403753.

47 X. Zhang, X. Gu and H. Huang, Low-Cost Nonfused-Ring Electron Acceptors Enabled by Noncovalent Conformational Locks, *Acc. Chem. Res.*, 2024, **57**, 981–991.

48 Q. Zhang, Z. Pei, A.-Y. Song, M. Qi, R. S. H. Khoo, C. Yang, T. Xia, C. Zhou, H. Mao, Z. Huang, S. Lai, Y. Wang, L. Z. Tan, J. A. Reimer, J. Zhang, M. L. Coote and Y. Liu, Manipulating Aromaticity to Redirect Topochemical Polymerization Pathways, *J. Am. Chem. Soc.*, 2025, **147**, 14715–14724.

49 C. Yang, J. Liu, R. S. H. Khoo, M. Abdelsamie, M. Qi, H. Li, H. Mao, S. Hemenway, Q. Xu, Y. Wang, B. Yu, Q. Zhang, X. Liu, L. M. Klivansky, X. Gu, C. Zhu, J. A. Reimer, G. Cui, C. M. Sutter-Fella, J. Zhang, G. Ren and Y. Liu, High-fidelity topochemical polymerization in single crystals, polycrystals, and solution aggregates, *Nat. Commun.*, 2025, **16**, 3498.

50 C. L. Anderson, H. Li, C. G. Jones, S. J. Teat, N. S. Settineri, E. A. Dailing, J. Liang, H. Mao, C. Yang, L. M. Klivansky, X. Li, J. A. Reimer, H. M. Nelson and Y. Liu, Solution-processable and functionalizable ultra-high molecular weight polymers *via* topochemical synthesis, *Nat. Commun.*, 2021, **12**, 6818.

51 T.-J. Wen, Z.-X. Liu, Z. Chen, J. Zhou, Z. Shen, Y. Xiao, X. Lu, Z. Xie, H. Zhu, C.-Z. Li and H. Chen, Simple Non-Fused Electron Acceptors Leading to Efficient Organic Photovoltaics, *Angew. Chem., Int. Ed.*, 2021, **60**, 12964–12970.

52 C. A. Hunter and J. K. M. Sanders, The nature of pi-pi interactions, *J. Am. Chem. Soc.*, 1990, **112**, 5525–5534.

53 Y. Chen, F. Bai, Z. Peng, L. Zhu, J. Zhang, X. Zou, Y. Qin, H. K. Kim, J. Yuan, L. Ma, J. Zhang, H. Yu, P. C. Y. Chow, F. Huang, Y. Zou, H. Ade, F. Liu and H. Yan, Asymmetric Alkoxy and Alkyl Substitution on Nonfullerene Acceptors Enabling High-Performance Organic Solar Cells, *Adv. Energy Mater.*, 2021, **11**, 2003141.

54 S. H. K. Paleti, S. Hultmark, J. Han, Y. Wen, H. Xu, S. Chen, E. Järsvall, I. Jalan, D. R. Villalva, A. Sharma, J. I. Khan, E. Moons, R. Li, L. Yu, J. Gorenflot, F. Laquai, C. Müller and D. Baran, Hexanary blends: a strategy towards thermally stable organic photovoltaics, *Nat. Commun.*, 2023, **14**, 4608.

55 H. Zhao, N. Prine, S. Kundu, G. Ma and X. Gu, Effect of Thermal Stress on Morphology in High-Performance Organic Photovoltaic Blends, *JACS Au*, 2024, **4**, 4334–4344.

56 S. Li, R. Zhang, M. Zhang, J. Yao, Z. Peng, Q. Chen, C. Zhang, B. Chang, Y. Bai, H. Fu, Y. Ouyang, C. Zhang, J. A. Steele, T. Alshahrani, M. B. J. Roeffaers, E. Solano, L. Meng, F. Gao, Y. Li and Z.-G. Zhang, Tethered Small-Molecule Acceptors Simultaneously Enhance the Efficiency and Stability of Polymer Solar Cells, *Adv. Mater.*, 2023, **35**, 2206563.

57 G. C. Welch, R. C. Bakus, S. J. Teat and G. C. Bazan, Impact of Regiochemistry and Isoelectronic Bridgehead Substitution on the Molecular Shape and Bulk Organization of Narrow Bandgap Chromophores, *J. Am. Chem. Soc.*, 2013, **135**, 2298–2305.

58 Z. B. Henson, G. C. Welch, T. Van Der Poll and G. C. Bazan, Pyridalthiadiazole-Based Narrow Band Gap Chromophores, *J. Am. Chem. Soc.*, 2012, **134**, 3766–3779.

59 G. C. Welch, L. A. Perez, C. V. Hoven, Y. Zhang, X.-D. Dang, A. Sharenko, M. F. Toney, E. J. Kramer, T.-Q. Nguyen and G. C. Bazan, A modular molecular framework for utility in small-molecule solution-processed organic photovoltaic devices, *J. Mater. Chem.*, 2011, **21**, 12700–12709.

60 X. Zou, G. Wen, R. Hu, G. Dong, C. Zhang, W. Zhang, H. Huang and W. Dang, An Insight into the Excitation States of Small Molecular Semiconductor Y6, *Molecules*, 2020, **25**, 4118.

61 Y.-X. Xu, C.-C. Chueh, H.-L. Yip, F.-Z. Ding, Y.-X. Li, C.-Z. Li, X. Li, W.-C. Chen and A. K.-Y. Jen, Improved Charge Transport and Absorption Coefficient in Indacenodithieno[3,2-*b*]thiophene-based Ladder-Type Polymer Leading to Highly Efficient Polymer Solar Cells, *Adv. Mater.*, 2012, **24**, 6356–6361.

62 C. Reichardt, Solvatochromic Dyes as Solvent Polarity Indicators, *Chem. Rev.*, 1994, **94**, 2319–2358.

63 Y. Shi, Y. Chang, K. Lu, Z. Chen, J. Zhang, Y. Yan, D. Qiu, Y. Liu, M. A. Adil, W. Ma, X. Hao, L. Zhu and Z. Wei, Small reorganization energy acceptors enable low energy losses in non-fullerene organic solar cells, *Nat. Commun.*, 2022, **13**, 3256.

64 J. H. Kim, T. Schembri, D. Bialas, M. Stolte and F. Würthner, Slip-Stacked J-Aggregate Materials for Organic Solar Cells and Photodetectors, *Adv. Mater.*, 2022, **34**, 2104678.

65 G. Zhang, X.-K. Chen, J. Xiao, P. C. Y. Chow, M. Ren, G. Kupgan, X. Jiao, C. C. S. Chan, X. Du, R. Xia, Z. Chen, J. Yuan, Y. Zhang, S. Zhang, Y. Liu, Y. Zou, H. Yan, K. S. Wong, V. Coropceanu, N. Li, C. J. Brabec, J.-L. Bredas, H.-L. Yip and Y. Cao, Delocalization of exciton and electron wavefunction in non-fullerene acceptor molecules enables efficient organic solar cells, *Nat. Commun.*, 2020, **11**, 3943.

66 D. Li, X. Zhang, D. Liu and T. Wang, Aggregation of non-fullerene acceptors in organic solar cells, *J. Mater. Chem. A*, 2020, **8**, 15607–15619.

67 N. J. Hestand and F. C. Spano, Expanded Theory of H- and J-Molecular Aggregates: The Effects of Vibronic Coupling and Intermolecular Charge Transfer, *Chem. Rev.*, 2018, **118**, 7069–7163.

68 N. Yao, J. Wang, Z. Chen, Q. Bian, Y. Xia, R. Zhang, J. Zhang, L. Qin, H. Zhu, Y. Zhang and F. Zhang, Efficient Charge Transport Enables High Efficiency in Dilute Donor Organic Solar Cells, *J. Phys. Chem. Lett.*, 2021, **12**, 5039–5044.

69 W. Yang, W. Wang, Y. Wang, R. Sun, J. Guo, H. Li, M. Shi, J. Guo, Y. Wu, T. Wang, G. Lu, C. J. Brabec, Y. Li and J. Min, Balancing the efficiency, stability, and cost potential for organic solar cells *via* a new figure of merit, *Joule*, 2021, **5**, 1209–1230.

70 S. Y. Kim, C. C. F. Kumachang and N. Y. Doumon, Characterization Tools to Probe Degradation Mechanisms in Organic and Perovskite Solar Cells, *Sol. RRL*, 2023, **7**, 2300155.

71 S. Rousseva, H. den Besten, F. S. van Kooij, E. L. Doting, N. Y. Doumon, E. Douvogianni, L. J. Anton Koster and J. C. Hummelen, Reaching a Double-Digit Dielectric Constant with Fullerene Derivatives, *J. Phys. Chem. C*, 2020, **124**, 8633–8638.

72 Y. Qiu, R. Peng, J. Shi, Z. Chen and Z. Ge, Revealing and Eliminating the Light-Soaking Issue in Metal Oxide-Based Inverted Organic Solar Cells, *Adv. Funct. Mater.*, 2023, **33**, 2300831.

73 P. Tiwana, P. Docampo, M. B. Johnston, L. M. Herz and H. J. Snaith, The origin of an efficiency improving ''light soaking'' effect in $SnO_2$ based solid-state dye-sensitized solar cells, *Energy Environ. Sci.*, 2012, **5**, 9566–9573.